Self-Potential Method to Assess Embankment Stability: A Study related to the Sidoarjo Mud Flow

Sungkono[1,*], Masithoh N. Wasilah[1], Yekti Widyaningrum[2], Wildan M. Hidayatullah[1], Fandi A. Fathoni[1] & Alwi Husein[3]

[1]Physics Department, Faculty of Sciences, Institut Teknologi Sepuluh Nopember, Jalan Arif Rahman Hakim, Surabaya 60111, Indonesia
[2]Physics Department, Universitas Bangka Belitung, Jalan Kampus Peradaban, Bangka Belitung, Indonesia
[3]Pusat Pengendalian Lumpur Sidoarjo, Jalan Gayung Kebonsari No. 50, Surabaya, 60235, Indonesia
*E-mail: hening_1@physics.its.ac.id

Highlights:

- Noise-Assisted Multivariate Empirical Mode Decomposition (NA-MEMD) can be used for qualitative interpretation of self-potential (SP) data.
- Continuous Wavelet Transform (CWT) analysis was applied to identify multiple anomaly sources from SP data.
- NA-MEMD and CWT were applied to SP data for qualitative and quantitative interpretations, respectively.
- The combination of NA-MEMD and CWT on SP data was used to identify the location of fractures and seepage in the LUSI embankment.
- The interpretation of the result was supported by direct current resistivity.

Abstract. The stability of an embankment is generally influenced by a number of factors, such as deformation, fractures, overtopping, seepage, etc. Fractures and seepage are commonly found in the LUSI (Sidoarjo mud flow) embankment. In this study, analysis of self-potential (SP) data was applied to identify fractures and seepage in the LUSI embankment. Noise-Assisted Multivariate Empirical Mode Decomposition (NA-MEMD) and Continuous Wavelet Transform (CWT) were applied to determine the location of seepage and fractures in the subsurface based on SP data. The results were correlated with the 2D direct current resistivity (DCR) method, which showed that both methods worked well and were compatible in detecting and localizing fracture and seepage in the LUSI embankment.

1 Introduction

Failure of the LUSI (the Sidoarjo mud flow) embankment is mainly caused by seepage. Seepage flows through cracks in the embankment body. The degree of

water seepage in earth-fill embankments can be identified using the self-potential (SP) method [1-4]. The SP method includes a passive method that measures the natural static voltage of the ground. This method only needs voltage sensitive measuring devices and two special electrodes to conduct measurements, making this method quite fast and simple to execute. The spatial distribution of the measured SP data can indicate possible anomalous water flow.

Generally, inversion is used to identify the locations (distance and depth) of sources causing SP anomalies. Forward modeling is required in the inversion process, where forward modeling of SP in the inversion process generates idealized bodies (example: sphere, cylinder, inclined sheet, inclined thick sheet) [5-9]. Several phenomena that disturb embankment stability can be approximated by simple geometrical models [3]: piping can be represented by a cylindrical body, internal erosion can be represented by a sphere, differential settlement can be represented by horizontal fractures, which can be represented by an inclined sheet. These assumptions cannot be used in general cases, because in some cases the sources of SP anomalies cannot be represented by idealized bodies but complex bodies are required [10]. Moreover, embankment instability is caused by a combination of several idealized bodies [3]. Thus, using a single idealized body model in the localization of SP sources has high ambiguitiy.

In order to locate instability in the LUSI embankment, the filtered adaptive method Noise-Assisted Multivariate Empirical Mode Decomposition (NA-MEMD) and Continuous Wavelet Transform (CWT) analysis were used. NA-MEMD removes noise from the SP data for a qualitative interpretation, while CWT determines the subsurface position of SP body anomalies for a quantitative interpretation. In order to identify anomaly sources, the CWT method does not need assumptions. Although seepage in the LUSI embankment generally occurs through fractures or rock pores in the embankment body, the CWT analysis of anomaly sources is assumption-free for determining the seepage positions. As most geophysical methods, SP suffers from inherent ambiguity. Consequently, in identifying the positions of SP body anomalies, uncertainty model solutions are needed [7,11]. CWT analysis can provide the uncertainty positions of SP anomaly sources.

2   Theory of Self-Potential

The principle of the SP method is to measure the natural potential that is formed in the subsurface by several mechanisms, namely mineralization (geobattery), electrochemical (liquid junction or diffusion), electrokinetic (streaming), and thermoelectric potential. Firstly, SP anomalies associated with the presence of ore deposits are caused by redox half-reactions [12] involving electron donors and electron acceptors. The resulting potential is called electrochemical potential

and generally causes strong SP anomalies (in the order of hundreds of millivolts). Secondly, SP anomalies related to different mobility of anions and cations in solutions with different concentrations are LUSI embankment called diffusion potential [13]. Thirdly, streaming potential related to the motion of ground water in porous rocks is caused by the pore pressure gradient or hydraulic head [1]. Generally, the streaming potential can have an amplitude from some millivolts to several hundred of millivolts. The thermoelectric potential occurs due to the thermal gradient inside the rock, where the thermal gradient increases the energy of the ions leading to a differential displacement between the ions, which generates an electrical current [13].

Furthermore, streaming potential with null total current density can be defined mathematically as follows [1,14,15]:

$$C = \frac{\nabla \varphi}{\nabla h} = -\frac{Q_v K}{\sigma_b} = -\frac{Q_v KF}{\sigma_f} \tag{1}$$

where F and C are the formation factor and the streaming potential coupling coefficient, respectively, while φ and h represent the electric potential (V) and hydraulic head (m), respectively. Furthermore, Q_v indicates the excess of electric charge per unit pore volume [C/m^3], σ_b and σ_f are the bulk and pore water electrical conductivity [S/m], respectively, and K is the hydraulic conductivity [m/s]. The equation has as a consequence that an upstream condition (the hydraulic head of the measurement electrode is located above the hydraulic head of the reference electrode) will produce negative SP anomalies on the surface and vice versa. Consequently, there are negative and positive SP anomalies for inflow and outflow, respectively.

Pressure is directly proportional to height. Consequently, using Eq. (1) it can be known that the streaming potential also depends on pressure. In general, fluid flows from high pressure to low pressure, which means that the location of water discharge (inflow in embankment seepage) will produce negative SP anomalies, while the direction of the fluid flow (outflow) has positive SP anomalies on the surface.

SP data can be disturbed by several types of noise [12], namely: 1) noise generated by different transient sources; 2) spatial noise associated with strong heterogeneity of the resistivity distribution in the near surface; 3) other artifacts associated with the non-polarizing electrodes themselves. Transient noise can be removed if a fixed dipole is used to record the electrical signals during mapping, while spatial noise can be filtered if measurements are made with high spatial

density and can be removed using several processing techniques (Fourier-, wavelet- and empirical mode decomposition-based filters). In addition, other artifacts can be corrected if the temperature is measured at the place where the self-potential measurements are carried out.

3   Study Area

Geologically, the LUSI area is part of the Brantas river system with the following rock sequence (from old to young): Ngimbang, Kujung, Tuban, Ngrayong, Wonocolo, Ledok, and Lidah formations. At the surface, the formation consists of alluvial deposits from the Brantas delta (in the north of the Porong river) and Quaternary volcanic tuff deposits (in the south of the Porong river). The alluvial delta is mainly derived from the Brantas river, which separates into two rivers, namely the Kali Mas river in the north and the Porong river in the south, in the form of alluvium, composed of gravel, sand, and silty clay [16].
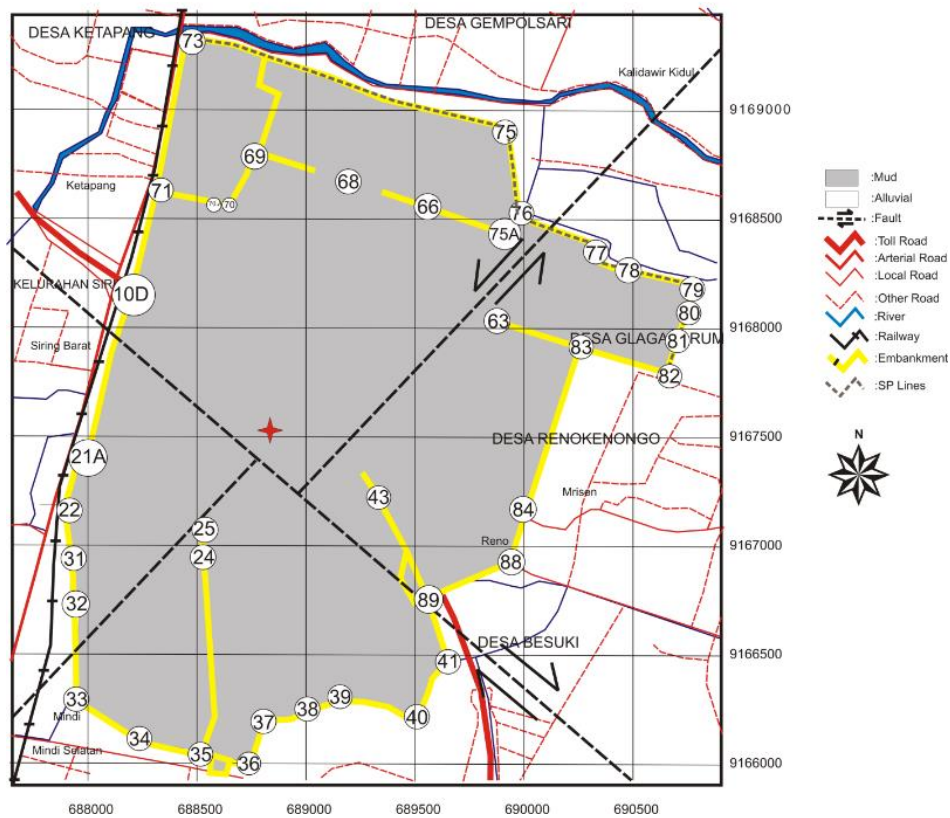

Figure 1 Geological map and structures in the LUSI area. Points with numbers are used to easily find positions in the LUSI embankment.

The LUSI embankment is the main embankment and is built on the outside of the affected area (Figure 1). The embankment was built in expansive soil with high resistivity. Construction was done in view of the LUSI mud eruption and the main goal was to protect the public and avoid greater losses to the state. The LUSI embankment was constructed over two faults, the Siring fault and the Watukosek fault (Figure 1). Nevertheless, the embankment is well constructed and has high standard penetration test (SPT), shear wave velocity, and resistivity [16-18]. In order to facilitate the reference to a point or a pond in the LUSI embankment, each position is denoted by 'P' followed by a number (for example: P79 for point 79).

Figure 1 shows the measurement of the SP data lines. Observation of the SP lines was focused on the north and northeast of the LUSI embankment, because these areas have highly collapse potential [19]. The embankment in the north and northeast parts was designed with thicknesses of 11 m and 5 m for the width of the top part (Figure 2) [20,21], but has been repaired each year (especially before the rainy season) to handle unstability. Consequently, P79 to P82 of the LUSI embankment was identified as being about 12 to 15 m thick in 2017 using integrated vertical electrical sounding and Rayleigh wave dispersion [19].
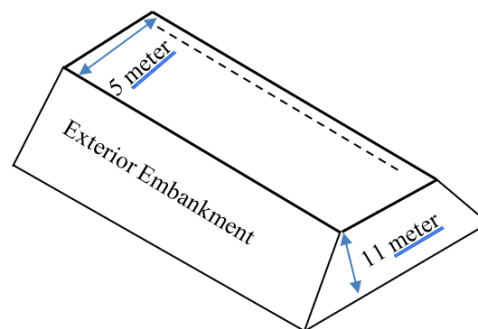

Figure 2 Dashed lines indicate the localization of the SP and DCR electrodes for each line at the crest of the dam.

Instability of the LUSI embankment is generally caused by three factors [16,19]: (1) vertical and horizontal deformations, which will eventually lead to changes of position of the embankment and cracks in the embankment; (2) the effects of fluid eruption in large quantities causing overtopping and seepage in the embankment; (3) the driving force of the LUSI mud flow or fluid on the embankment, causing embankment failure due to the transformation of the potential energy of the mudslide into kinetic energy. Moreover, the latter generally contributes to collapse of the embankment in the rainy season (especially when it rains a lot).

In this study, the potential difference (PD) method was used, where one electrode is fixed to a base station and another one is moved at a regular interval. Measurement of the self-potential signals was carried out with a digital voltmeter and non-polarizing Cu/CuSO4 electrodes. The spacing between the SP readings was 5 m and the measured data were corrected [12]. The NA-MEMD and CWT methods were applied to correct the SP data for qualitative and quantitative interpretation, respectively.

Furthermore, the direct current resistivity (DCR) method was used to measure the same line as SP (Figure 2) in order to integrate both data. Measurements of 2D DCR are generally used to determine the true electrical resistivity of the subsurface. The DCR method measures the electrical resistivity distribution of the subsurface using a DC current. The current is transmitted into the ground with two electrodes (A and B) and the potential difference between a second pair of electrodes (M and N) is measured. Several electrode arrays can be used to determine subsurface resistivity, including Wenner, Schlumberger, dipole-dipole and pole-pole arrays. The Wenner configuration was selected for measuring with the DCR method.

4   Data Processing

4.1   Self-Potential Data

4.1.1   Noise-Assisted Multivariate Empirical Mode Decomposition (NA-MEMD)

In this study, Noise-Assisted Multivariate Empirical Mode Decomposition (NA-MEMD) [22,23] was used to filter the SP data. This method is able to eliminate mode mixing in the multivariate empirical mode decomposition (MEMD) algorithm. Thus, the method is suitable for filtering geophysical data [24]. It was used to remove linear trends from the data, which were generally correlated with electrode drift and with base slope and level. Furthermore, the method also reduced high frequency noise that reflects the telluric effect and was associated with the very heterogeneous nature (resistivity distribution) of the shallow subsurface.

The NA-MEMD method operates on SP data and several white Gaussian noise (WGN) channels with a certain amplitude was added to separate channels from the SP data. Further, Multivariate Empirical Mode Decomposition (MEMD) [25] was applied to decompose the SP data and several WGN channels to obtain several multivariate intrinsic mode functions (IMFs). Several channels of the multivariate IMFs corresponding to WGN were excluded, while the other

channels were IMFs of the SP data. Furthermore, some IMFs were selected for reconstructing free noise of SP data, while a IMFs reflected a linear trend and IMFs associated with the telluric effect and the very heterogeneous resistivity of the shallow subsurface were excluded. The filtered SP data were used for qualitative interpretation, the result of which was compared with the CWT and DCR results.

4.1.2   Continuous Wavelet Transform (CWT)

Continuous Wavelet Transform (CWT) can be applied to accurately calculate the position (depth and distance) of sources bodies of potential field anomalies (gravity, magnetic, and self-potential data) [26,27]. The wavelet transform is a signal analysis method that uses simultaneous characterization of a signal in the time and frequency or the space and wave number domain. CWT is obtained by convolution or cross-correlation between a signal (in this study SP measured data) $f(x)$ and multiple scales (multiple σ) of wavelets g_n with different translation parameters x'. The wavelet transform is described in detail in [28,29]. Mathematically, the wavelet transforms results, $Wf(x',\sigma)$, can be expressed as follows:

$$W[g_n, f](x',\sigma) = \sigma^{-n} \int_{-\infty}^{\infty} g_n([x-x']/\sigma) f(x) dx \qquad (2)$$

where $g_n([x-x']/\sigma)$ denotes a wavelet that has spatial support centered at x' and is proportional to σ. Using the properties of the wavelets, the scale parameter (σ) plays the role of the physical dimension depth (Z), while the translation parameter is the equivalent of position x [30]. The scale parameter is proportional to the dilation parameter [30]. Furthermore, the scale is described as the window size of the wavelet. A small scale means a detailed view, which will increase the resolution in the same time, and vice versa.

In order to increase efficiency, the CWT is processed in the wavenumber u domain (frequency domain in the spatial function). Thus, this process needs fast Fourier transforms. Generally, the derivative of order n of the Poisson kernel family and their Hilbert transforms are used as wavelets, horizontal and vertical, respectively. The wavelet equation is as follows:

$$H_n(u) = (2\pi u)^n \exp(-2\pi|u|)$$
$$V_n(u) = -2\pi|u|(2\pi ui)^{n-1} \exp(-2\pi|u|) \qquad (3)$$

where u denotes the wavenumber of the spatial variable x.

Using the convolution concept, the wavelet transform of a signal using several scales has the following properties:

1. High frequency (wavenumber) in low scales and vice versa. This has two consequences, namely: a high frequency signal is clearly visible in the low scales, and vice versa, and the wavelet transform can act as a filtering process.
2. It contains properties of the signal and wavelet is used in this process.

Based on the properties of the wavelet transforms, the SP and potential data indicate subsurface anomaly source that are visible in high and low scales. The wavelet transform property is different from the noise property disturbing the SP and potential data [27,31].

Furthermore, CWT can identify singularities very well [32]. A singularity is described by extrema lines in the matrix wavelet transform results (wavelet transform modulus maxima lines, WTML). For identifying the source of an anomaly, two or more extrema (minima and maxima) lines are needed, where at least one line is of maxima and one line of minima [27]. Generally, each body source of self-potential anomalies will generate a singularity in the CWT results.

Mauri *et al.* [26] have shown that the dilation value is considered as the space above the ground surface (z > 0) and as projection below the ground surface (z < 0). The lines of extrema converge at z < 0 in a cone-shaped structure toward the singularity. The convergence position of the extrema represents the position (depth and distance) of the SP anomaly source. A more clear description of this methodology can be found in References [26,27,33].

In order to investigate the accuracy of CWT to predict positions of seepage (fluid flow) disturbing embankment stability, this study used a combination of real and imaginary wavelets based on the Poisson kernel function. The real wavelets of the Poisson family using this process are the second horizontal derivative and the third vertical derivative, while the imaginary wavelets are the third horizontal derivative and the second vertical derivative, as discussed in [26].

Variations and errors in depth calculations are caused by three main sources [27]. Firstly, noise in the data (due to a heterogeneous medium) will distort the lines of the extrema for small values of dilation. Consequently, this will affect the point of convergence. Secondly, the error due to the heterogeneous medium, which is calculated based on the quality of the best fit of the cone-shaped structure. Thirdly, the sampling step has a significant impact on the measured signal and the signal may characterize the source. The error due to measurement noise can be further limited by processing the signal with several wavelets (more than one) in order to statistically constrain the depth.

4.2   Resistivity Data

The DCR data were analyzed using the L1-norm optimization method. L1-norm's error approach is less sensitive to noise levels and produces fewer artifacts [34], while L1-norm's modeling commonly gives better imaging results for the contrast of the model parameter than smoothness constrained least-squares (L2-norm) inversion [35,36]. Inversion using L1-norm is done to minimize the objective function, as follows:

$$\phi = \left| R_d \left(d_{obs} - d_{cal} \right) \right| + \lambda_i \left| R_m W \Delta r_i \right| \tag{4}$$

where R_d and R_m denote the weighted misfit and data roughness, respectively, J indicates the Jacobian matrix of the partial derivatives, while W describes the roughness filter. Further, d_{obs} and d_{cal} are the observed and calculated data, and Δr_i indicates the changed model parameters for the ith iteration.

The Lagrange multiplier for each iteration (λ_i) is used to minimize model roughness and to stabilize the inversion process. A simple approach to solving L1-norm based optimization is the iteratively reweighted least-squares method (IRLS) [34,35]. In the IRLS algorithm, both R_d and R_m are iteratively calculated [36].

5   Result and Discussion

SP and DCR data were acquired in the rainy seasons. The pond condition for each line is presented in Figure 3. The figure shows that generally the pond contained water, except at line P76-P77. This condition was used to help in the interpretation of the processed SP and DCR results.

In order to locate anomalies, the NA-MEMD approach was applied to the SP data. Figure 4 shows SP data decomposition into 5 IMFs, where the last IMF indicates the trend of the data. This trend correlates with electrode drift and topography (Figure 4). Thus, the last IMF must be excluded from the SP data reconstruction.

The first and second IMFs show transient data, which may be caused by strong heterogeneity of the resistivity variation in the shallow subsurface and may also have been disturbed by transient sources, such as the telluric effect due to transient current flow in the ionosphere, lightning, large cumulus clouds, etc.

Figure 3 Pond (point) condition of each line, a) P79-P82; b) P78-P79; c) P76-P77; d) P75-P73; e) P75A-P75. Each pond contained fluid, except P76-P77.
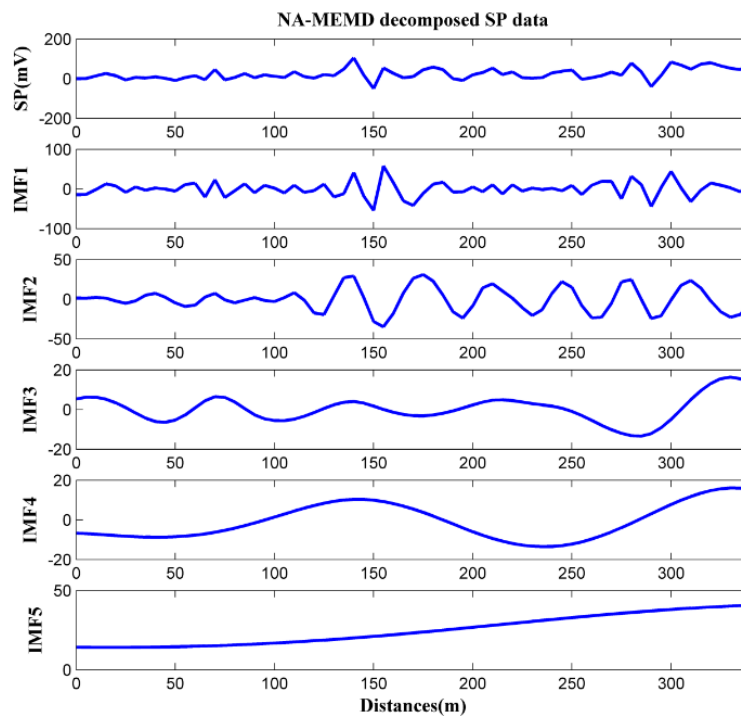

Figure 4 SP data decomposed using NA-MEMD into five IMFs.

Furthermore, the last, the first and the second IMF must be removed. Consequently, in order to reconstruct the SP anomalies (filtered SP), IMF 3-IMF4 can be summed as in Figure 5. This figure shows that compared with SP measurement, the SP anomalies were improved by removing the last IMF and transient data compression by excluding the first and the second IMF. These steps were performed for all SP measurement lines. Further, the filtered SP data were interpreted qualitatively (based on the properties of the SP anomalies) and quantitatively (wavelet multiscale processing).
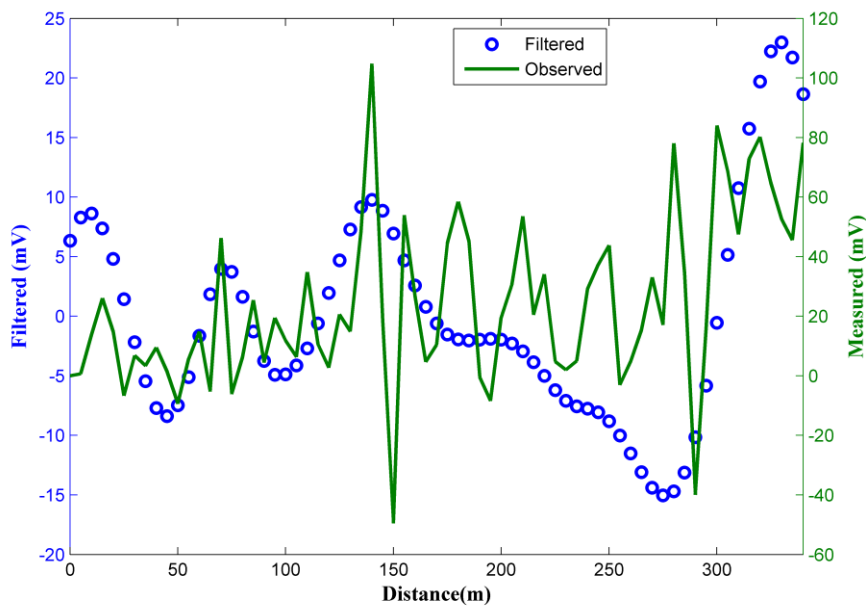

Figure 5 Comparison of measured SP and filtered SP using the NA-MEMD approach.

As described in Eq. (1), the qualitative interpretation of self-potential anomalies of streaming potentials for identifying seepage is easy, where seepage is generally shown by negative SP anomalies [14,15,37,38]. In addition, the relative intensity of the discharge is demonstrated by the amplitude of the anomalies. The SP data filtered using the NA-MEMD algorithm were applied in the qualitative interpretation for identifying seepage positions.

In the quantitative interpretation of the SP anomalies, the measured SP data were analyzed using wavelet multiscale analysis to estimate the depth of the source responsible for the measured SP anomalous field [26,27]. In this study, the second and third orders of the vertical and horizontal derivatives of the Poisson family were used to provide the uncertainty positions of the subsurface anomalies. For

this process, the MWTmat software [26] was used to analyze the measured self-potential field. In the software, the SP data were processed using CWT to identify the minimum and maximum singularities. Further analysis of both singularities was done to identify the sources of the SP anomalies. As a quality check of the results for the source positions, only positions with at least two of the four wavelet analyses were considered significant. For each wavelet and profile a position was obtained by estimating the best fit of the cone-line structure [26].

The convergence of the line's extrema through intersection point $z < 0$ gives the depth of the SP source. As shown in Figure 6, CWT analysis was applied to the SP data measured at P79-P82 (Figure 5) using the second order of the vertical derivative of the Poisson family.

The figure shows that sources of SP anomalies can be identified by singularity analysis, where negative and positive singularities (dashed lines) will meet at a point (diamond) and form a cone. The points correlate to the positions of the SP anomaly sources. The results were divided into four groups of SP anomaly sources, where each group was identified through two or more singularities (see Figure 6). Furthermore, the data were also analyzed using another wavelet, which is not presented here.
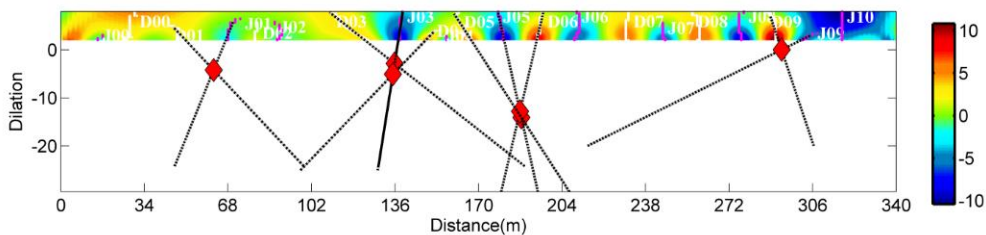

Figure 6 CWT analysis of measured SP to determine anomaly sources.

For each estimated depth, the associated error is based on the quality of the best fit. The final localization of each source (horizontal and vertical) was based on the depths and distances of all solutions from the analyzed results and their associated uncertainty (σ). The analysis results for all of the measured SP data are presented in Table 1. It shows the CWT analysis result consisting of the depth and position of each SP source. The WTML in the CWT analysis of the SP data cannot determine the nature of the object associated with an SP anomaly. In order to describe the nature of the SP anomaly object, dipolar tomography (advanced complex CWT analysis of the SP data) and SP data inversion using the finite element approach can be used [31,39-41].

Table 1   Source depths (Z) and positions (X) Estimated by CWT of self-potential data in the LUSI embankment for several lines.

Structure	Number of Wavelets	X	σX	Z	σZ
Line P79-P82					
S1	4	67.3967	6.5865	-10.2437	9.550729
S2	4	190.4354	9.231651	-65.1711	15.99827
S3	4	138.3866	4.136642	-15.6224	5.483529
S4	4	273.5462	20.5845	-32.2226	9.073569
Line P78-P79					
SS1	4	194.3154	0.93842	-20.2692	4.851243
SS2	4	85.26599	2.699981	-23.3347	8.868472
SS3	4	32.88858	0.72523	-4.91201	3.794171
SS4	4	239.0813	0.765973	-22.8812	3.88584
SS5	3	281.9847	0	-7.94234	7.9434
SS6	3	352.4498	30.30011	-8.24386	7.547819
SS7	4	325.5904	5.60797	-44.0136	7.640628
SS8	4	146.5408	3.638915	-36.7046	19.04271
Line P76-P77					
WK1	3	81.54776	15.03222	-7.55414	5.48696
WK2	3	108.4507	3.917961	-67.2183	21.66722
WK3	3	197.961	14.14983	-5.76768	2.884647
WK4	3	256.6205	3.27331	-39.1937	12.449
WK5	2	191.0173	11.11475	-29.5334	7.198908
WK6	2	36.26095	2.56701	-3.97696	4.493881
Line P75A-P75					
KD1	3	222.7747	0.345972	-8.06587	0.807549
KD2	4	44.20035	0.679158	-10.3666	1.859948
KD3	4	160.4179	3.036411	-31.574	12.09849
KD4	4	290.9196	7.335863	-68.47	15.65895
KD5	3	102.5827	1.167678	-28.991	2.241301
Line P75-P73					
KT1	3	88.6605	2.28848	-4.64522	2.188764
KT2	4	275.451	6.781233	-61.3532	25.06461
KT3	4	506.921	1.632278	-14.9403	6.094641
KT4	3	607.0037	6.992968	-50.4533	18.28238
KT5	3	592.8443	32.07147	-4.23121	4.086568
KT6	2	731.802	18.39118	-1.40786	2.230054
KT7	2	420.1123	3.609299	-19.1776	6.172374

Note: Column 2 contains the number of wavelets used in the CWT calculation to locate the source depths and positions for each line. Depth and position are in meters. σ is the standard deviation to describe the result uncertainty.

As calibration, the analysis result of SP was compared with 2D imaging from the DCR method measured over the same lines. The DCR method was analyzed to minimize the L1-norm model and errors (Eq. (4)) using the IRLS method. The method is good to minimize tail errors and properly reconstruct the model of the embankment (the difference in resistivity in the embankment and under the embankment was assumed to be large).

5.1 Line P79-P82

Figure 7 demonstrates the correlation between SP anomalies, positions sources and their uncertainty estimated by CWT analysis, and the resistivity of the subsurface at line P79-P82. At this line, the thickness of the embankment is estimated around 10 to 15 m, as identified by the first resistivity layer and supported by Rayleigh wave analysis [18,19]. The low resistivity in the first layer indicates seepage in the embankment, which is correlated to negative SP anomalies. Thus, the SP anomalies can be used to determine seepage positions.
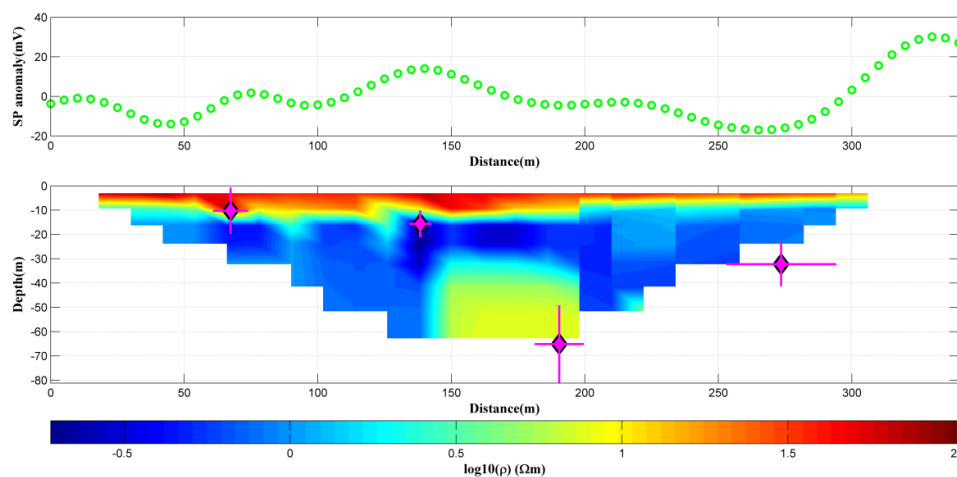

Figure 7 (a) Filtered SP anomalies (mV) and (b) 2D resistivity model estimated by DCR method and source positions of SP anomalies (diamonds) for P79-P82 of the LUSI embankment, Sidoarjo, Indonesia. Lines indicate a fracture or fault interpreted by DCR imagery.

The CWT of the SP data at this line identified four groups (Figure 7 and Table 1) that characterize four sources. Each anomaly controls a different area with uncertainty less than 21 m for position and 16 m for depth. Furthermore, the data were inverted using global optimization methods [4,42,43], where the results suggest that all the anomaly bodies at this line are horizontal cylinders. The anomalies can be interpreted as piping or seepage [3]. Moreover, seepage sources were also identified through CWT processing of SP anomalies, namely S1, S3, and S4.

Furthermore, the negative SP anomalies at 0-70 m, 80-110 m, and 170-250 m were considered near-surface fractures correlated with S1, S2, and S4, respectively. Fractures at S1 and S2 were clearly mapped in the 2D DCR

inversion result, while for S4 the fracture could not be identified from the 2D DCR analysis, but it was clearly revealed by inversion of the VLF-EM data [19] and by the GPR method [44]. This may be caused by the measurement point at around 170-250 m distance being limited (the observed data are based on the length of the embankment). The fracture network at this line is the result of deformation. This line has a high rate of vertical deformation as was demonstrated by the total station data analysis [19].

5.2   Line P78-P79

In order to know the cause of potential instability of the embankment at this line, qualitative and quantitative interpretations of the SP anomalies were applied. As described above, the qualitative interpretation is applied to presume seepage positions from the SP anomalies. During the measurements of the SP and DCR methods, the embankment was being repaired to increase the height and strength of the dikes. The thickness of the embankment at this line was around 12 m. Consequently, the first layer of the embankment, which is made of compacted earth fill, normally has higher resistivity than the second layer. Nevertheless, if the first layer is disturbed by fluid (seepage), the embankment will have low resistivity.

Figure 8 shows negative SP anomalies in several locations, such as at 0-50, around 100 m and 200 m, and at 175-215 m distance. If we compare the SP anomalies with 2D resistivity, seepage not always correlates to negative anomalies, as it can be seen around 250 m distance. In that location the SP anomalies were not only an effect of seepage but also of fracture (complex sources). Thus, the seepage position is difficult to identify through qualitative analysis. Furthermore, CWT analysis should be applied to identify the source of the SP anomalies.

A CWT analysis was conducted to determine the minimum and maximum singularities to estimate the sources of the SP anomalies. At this line, the anomalies indicated structures in 8 different groups. These groups reflect 8 different sources (Figure 8 and Table 1).

The sources of SP anomalies that can be seen in the near surface (in the embankment) were at SS5 (281.98 m distance) and SS6 (352.45 ± 30.30 m distance), where pores were the media of seepage. Furthermore, those at SS2 (85.27 ± 2.70 m distance), SS8 (146.54 ± 3.64 m distance), SS1 (194.32 ± 0.94 m distance), and SS4 (239.08 ± 0.77 m distance) can be considered faults. Faults also disturb embankment stability because water can seep in through the embankment. Fractures SS2 and SS8 were also revealed in the VLF-EM imaging

[19]. Thus, the seepage at this line may be caused by fractures and pores in the embankment.
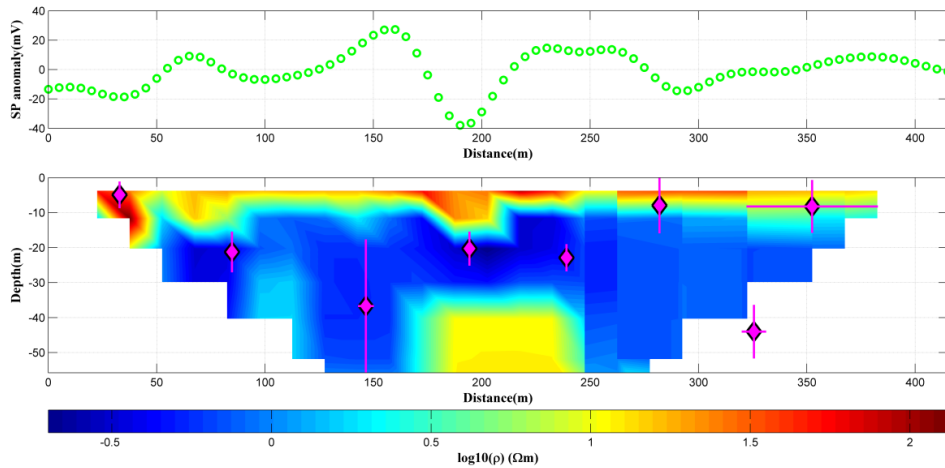

Figure 8 The same description as Figure 7 but for line 78-79.

5.3   Line P76-P77

Figure 1 shows that the measurements of the SP and DCR methods at line P76-P77 were taken over the Watukosek fault, where the fault is close to P76. The thickness of the embankment at this line was around 11-12 m. During the measurements, the pond at line P76-P77 was not filled with fluid. Consequently, in the rainy season, the fault or fracture will contain fluid and have low resistivity.

The CWT analysis of the SP data indicated structures in six different groups, which characterize six sources of SP anomalies (Figure 9 and Table 1). Figure 9 is a comparison between the SP and the DCR analysis results. Negative SP anomalies at a distance of 75-190 m correlate with low resistivity anomalies in the near surface (embankment), where the positions contain some structures. The structures are assumedly fractures or faults breaking through the embankment material. The structure is considered a water-filled fracture.

In addition, if we compare Figure 1 with Figure 9, the Watukosek fault system is correlated to WK2 (108.45 ± 3.92 m distance) in the CWT result of the SP anomalies and has low resistivity around both [45]. Fractures were also found at WK5 (191.02 ± 11.11 m distance) and WK6 (36.26 ± 2.57 m distance) consistent with low resistivity. WK5 and WK2 were also identified using VLF-EM imaging [19].

Another anomaly, WK1 (81.55 ± 15.03 m distance) is located in a 'near' fracture, which may be an uncertainty effect in the CWT analysis. The last anomaly, WK3 (197.96 ± 14.15 m distance) is considered porous rock containing fluid and has relatively low resistivity. Furthermore, the low resistivity anomaly from DCR located around 150 m distance was not identified using CWT, but the NA-MEMD result shows a small peak.
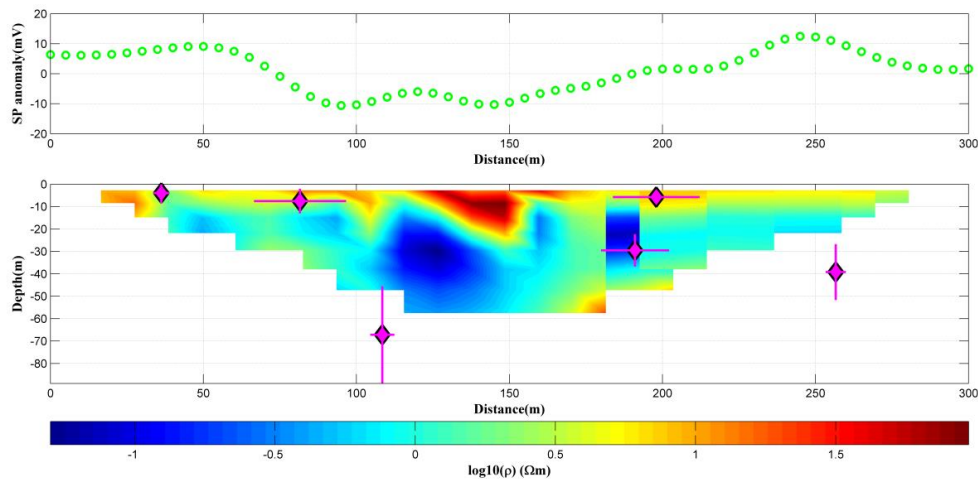

Figure 9 The same description as Figure 7 but for line 76-77.

5.4   Line P75A-P75

The measurements of the SP and DCR methods were done while the pond at this line was filled with fluid. Thus, fractures in the embankment would have been filled with fluid. Consequently, the fracture had lower resistivity than the embankment. The embankment at this line was estimated around 10 m (at a different height than P76), where during the measurement the embankment was under construction.

Figure 10 shows that the amplitude of the negative anomalies of the SP data found around 200-265 m distance was high. The negative SP zone values indicate probable paths of seepage in the downstream direction. If we compare this with DCR resistivity, seepage filling the fracture was shown by the low resistivity zone. The other seepage position could not be identified through qualitative analysis. This may be caused by the seepage position being close to other anomaly sources (for example fractures).
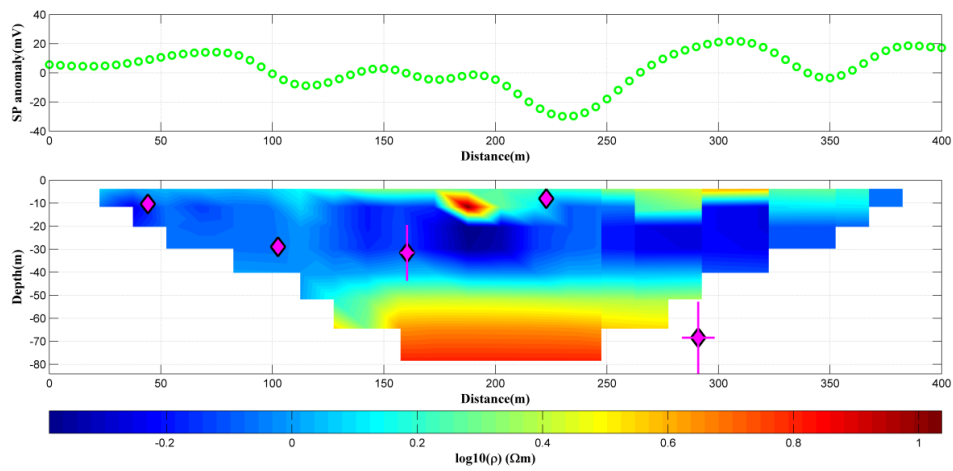
Figure 10 The same description as Figure 7 but for line 75A-75.

Figure 11 Internal erosion on 5 October 2018 is at around 150 to 250 m distance from P75A [46]. This means internal erosion caused by seepage.

CWT was also applied to the measured SP data to identify the position of each SP anomaly source. The CWT result indicated five groups, which characterize five sources of SP anomalies (Table 1 and Figure 10). The first source, KD1 (222.77 ± 0.35 m distance), may correspond to seepage sources, while the second

anomaly, KD2 (44.20 ± 0.67 m in distance), is a fluid outlet. Both sources were supported by the 2D resistivity data, with low resistivity in those positions. The anomalies were probably caused by structures (fractures) as denoted by KD1. Thus, the water saturated in this position passed through the fracture. Furthermore, Figure 11 shows slide embankment or internal erosion in this area on October 5, 2018 [46], which is correlated to negative SP anomalies (200-265 m distance) and may be caused by seepage in the embankment.

Furthermore, KD3 (160.42 ± 3.04 m distance) and KD5 (102.58 ± 1.17 m distance) as sources of SP anomalies were predicted as fractures based on the slightly different resistivity around both positions. Both fractures probably are not affected seepage, because they are relatively deep. Similar to KD3 and KD5, KD4 (290.92 ± 7.34 m in distance) may be considered a fracture, although the DCR inversion result did not reach to this position. The interpretation was based on the geological condition, where the area is controlled by a high rate of deformation. The deformation is mainly caused by mud loading and collapse of the overburden due to the removal of mud from the subsurface.

5.5   Line P75-P73

During the SP and DCR measurements, the embankment was being reinforced, where the embankment part consisted of two parts. Firstly, P75-P74 is relatively new, with a thickness of around 8-10 m. Secondly, P74-P73 is relatively old, with a thickness of around 11 m. Consequently, the second part of the embankment is more compact than the first. This condition is reinforced by the 2D resistivity as the inversion result of the DCR data (Figure 12). The pond at both parts of the embankment contained fluid from mud eruption (75% fluid and 25% solid) and rainwater.

Seepage assessment is indicated by the position of negative anomalies values. At line P75-P73 there are negative anomalies with potential values between -28 to -40 mV at 0-150 m and 595-795 m distance. The potential value was clearly measured in the electrical field, possibly caused by seepage flow. Furthermore, in order to know the depth of the SP anomalies, the CWT method was applied, which is resulted in five groups (Figure 12 and Table 1), indicates five sources.

The source of the negative anomaly at 0-150 m distance is denoted and interpreted as KT1 and seepage, respectively. This result was supported by the qualitative interpretation and low resistivity anomalies. Using the DCR inversion result, seepage through porous rock in this position was assumed. The deep source of SP anomalies denoted as KT2, probably indicates a fracture or a fault, where the source was demonstrated by contrast resistivity in the inversion result of the DCR data. The fracture assumedly are not affected by seepage in the embankment because its position is relatively deep. Furthermore, the sources of SP anomalies

denoted as KT3-KT7 are indicated as seepage through the near surface of a fracture (low resistivity in the near surface).
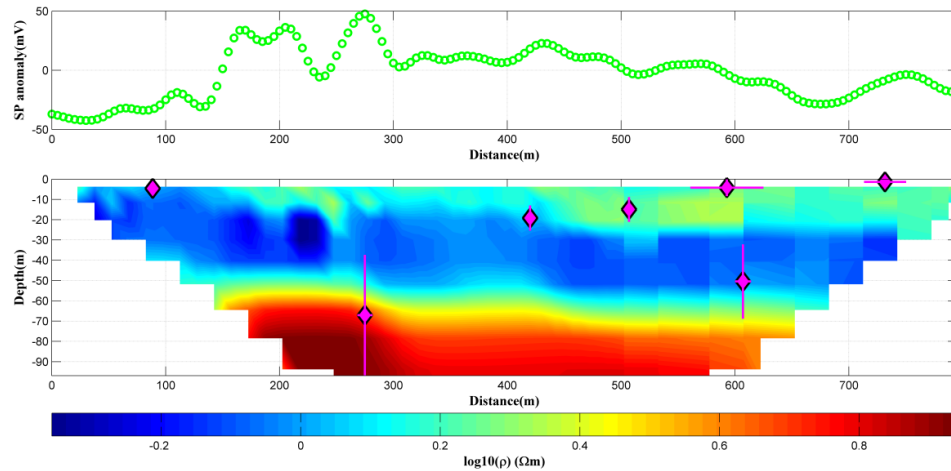

Figure 12 The same description as Figure 7 but for line 75-73.

6   Conclusions

Embankment stability can be disturbed by fluid. In this paper, the cause of embankment instability was identified using the SP method. Interpretation of measured SP data is difficult, because the data represent several different sources, which can potentially distort subsurface anomalies. NA-MEMD was applied to improve the SP data by decomposing the data and selecting several IMFs to represent the SP anomalies. This process is called SP data filtering using NA-MEMD. The filtering result is easy to use to identify seepage positions. Seepage is indicated by negative SP anomalies. This result is supported by low resistivity in the embankment. Furthermore, CWT was also applied to the SP data to determine the positions of SP anomaly sources. The result showed that the anomalies from the SP analysis were similar to those from the 2D resistivity analysis, where the anomalies were assumed to be faults or fractures and seepage through fractures and pores. The SP method is easy to implement, simple to interpret and fast in measurement. In the future, the SP method will be used to assess the stability of the LUSI embankment.

References

[1]   Ikard, S.J., Revil, A., Schmutz, M., Karaoulis, M., Jardani, A. & Mooney Mooney, M., *Characterization of Focused Seepage through an Earthfill Dam Using Geoelectrical Methods*, Groundwater, **52**(6), pp. 952-965, Nov. 2014. DOI: 10.1111/gwat.12151.

[2]   Minsley, B., Burton, B., Ikard, S. & Powers, M., *Hydrogeophysical Investigations at Hidden Dam*, Raymond, California, USGS Staff – Published Research, Jan. 2011. http://digitalcommons.unl.edu/ usgsstaffpub/517.

[3]   Rozycki, A., Ruiz, Fonticiella, J.M. & Cuadra, A., *Detection and Evaluation of Horizontal Fractures in Earth Dams Using the Self-Potential Method*, Engineering Geology, **82**(3), pp. 145-153, Jan. 2006. DOI: 10.1016/j.enggeo.2005.09.013.

[4]   Sungkono & Warnana, D.D., *Black Hole Algorithm for Determining Model Parameter in Self-Potential Data*, Journal of Applied Geophysics, **148**, pp. 189-200, Jan. 2018. DOI: 10.1016/j.jappgeo.2017.11.015.

[5]   Biswas, A. & Sharma, S.P., *Resolution of Multiple Sheet-Type Structures in Self-Potential Measurement*, J. Earth Syst. Sci., **123**(4), pp. 809-825, Jun. 2014. DOI: 10.1007/s12040-014-0432-1.

[6]   Biswas, A. & Sharma, S.P., *Optimization of Self-Potential Interpretation of 2-D Inclined Sheet-Type Structures Based on Very Fast Simulated Annealing and Analysis of Ambiguity*, Journal of Applied Geophysics, **105**, pp. 235-247, Jun. 2014. DOI: 10.1016/j.jappgeo.2014.03.023.

[7]   Biswas, A. & Sharma, S.P., *Interpretation of Self-Potential Anomaly Over Idealized Bodies and Analysis of Ambiguity Using Very Fast Simulated Annealing Global Optimization Technique*, Near Surface Geophysics, **13**(2), pp. 179-195, 2015. DOI: 10.3997/1873-0604.2015005.

[8]   Biswas, A. & Sharma, S.P., *Interpretation of Self-Potential Anomaly Over 2-D Inclined Thick Sheet Structures and Analysis of Uncertainty Using Very Fast Simulated Annealing Global Optimization*, Acta Geod Geophys, **52**(4), pp. 439-455, Dec. 2017. DOI: 10.1007/s40328-016-0176-2.

[9]   Monteiro Santos, F.A., *Inversion of Self-potential of Idealized Bodies' Anomalies Using Particle Swarm Optimization*, Computers & Geosciences, **36**(9), pp. 1185-1190, Sep. 2010. DOI: 10.1016/j.cageo. 2010.01.011.

[10] Patella, D., *Introduction to Ground Surface Self-Potential Tomography*, Geophysical Prospecting, **45**(4), pp. 653-681, Jul. 1997. DOI: 10.1046/ j.1365-2478.1997.430277.x.

[11]   Fernández-Martínez, J.L., García-Gonzalo, E. & Naudet, V., *Particle Swarm Optimization Applied to Solving and Appraising the Streaming-Potential Inverse Problem*, Geophysics, **75**(4), pp. WA3-WA15, Jul. 2010. DOI: 10.1190/1.3460842.

[12]   Revil, A. & Jardani, A., *The Self-potential Method: Theory and Applications in Environmental Geosciences*, Cambridge: Cambridge University Press, 2013.

[13]   Sharma, P.V., *Environmental and Engineering Geophysics*, Cambridge: Cambridge Univ. Press, 1997.

[14]   Bolève, A., Vandemeulebrouck, J. & Grangeon, J., *Dyke Leakage Localization and Hydraulic Permeability Estimation through Self-Potential and Hydro-Acoustic Measurements: Self-Potential 'Abacus' Diagram for Hydraulic Permeability Estimation and Uncertainty Computation*, Journal of Applied Geophysics, **86**, pp. 17-28, Nov. 2012. DOI: 10.1016/j.jappgeo.2012.07.007.

[15]   Grangeon, J.R., Boleve, A., Sanders, J.W. & Glaser, S.D., *Self-Potential Investigation of Moraine Dam Seepage*, Journal of Applied Geophysics, **74**(4), pp. 277-286, Aug. 2011. DOI: 10.1016/j.jappgeo.2011.06.014.

[16]   Sungkono, Husein, A., Prasetyo, H., Bahri, A.S., Monteiro Santos, F.A. & Santosa, B.J., *The VLF-EM Imaging of Potential Collapse on the LUSI Embankment*, Journal of Applied Geophysics, **109**, pp. 218-232, 2014. DOI: 10.1016/j.jappgeo.2014.08.004.

[17]   Husein, A., Santosa, B.J. & Bahri, A.S., *Seepage Monitoring of an Embankment Dam Using Resistivity Method: A Case Study of LUSI Mud Volcano P.79 - P.82 Embankment*, Applied Mechanics and Materials, **771**, pp. 213-217, Instrumentation and Measurement Systems, pp. 213-217, 2015.

[18]   Laby, D.A., Sungkono, Santosa, B.J. & Bahri, A.S., *RR-PSO: Fast and Robust Algorithm to Invert Rayleigh Waves Dispersion*, Contemporary Engineering Sciences, **9**, pp. 735-741, 2016. DOI: 10.12988/ces. 2016.6685.

[19]   Sungkono, Feriadi, Y., Husein, A., Prasetyo, H., Charis, M., Irawan, D., Rochman, J.P.G.N., Bahri, A.S. & Santosa, B.J., *Assessment of Sidoarjo Mud Flow Embankment Stability Using Very Low Frequency Electromagnetic Method*, Environmental Earth Sciences, **77**(196), 2018. DOI: 10.1007/s12665-018-7333-6.

[20]   Team Work of Operational Planning, *TTG and BM Monitoring Activity*, Sidoarjo Mud Volcano Agency, Reports of Year-end, 2013. (Text in Indonesian)

[21]   Team work of Operational Planning, *TTG and BM Monitoring Activity*, Center of Mud Volcano Control, Reports of Year-end, 2015. (Text in Indonesian)

[22] Rehman, N.U., Park, C., Huang, N.E. & Mandic, D.P., *EMD Via MEMD: Multivariate Noise-Aided Computation of Standard EMD*, Advances in Adaptive Data Analysis, **5**(2), 1350007, Apr. 2013. DOI: 10.1142/S179 3536913500076.

[23] Rehman, N.U. & Mandic, D.P., *Filter Bank Property of Multivariate Empirical Mode Decomposition*, IEEE Transactions on Signal Processing, **59**(5), pp. 2421-2426, 2011. DOI: 10.1109/TSP.2011.2106779.

[24] Sungkono, Bahri, A.S., Warnana, D.D., Monteiro Santos, F.A. & Santosa, B.J., *Fast, Simultaneous and Robust VLF-EM Data Denoising and Reconstruction via Multivariate Empirical Mode Decomposition*, Computers & Geosciences, **67**, pp. 125-137, 2014. DOI: 10.1016/j.cageo.2014.03.007.

[25] Rehman, N.U. & Mandic, D.P., *Multivariate Empirical Mode Decomposition*, Proc. R. Soc. A, **466**(2117), pp. 1291-1302, 2010. DOI: 10.1098/rspa.2009.0502.

[26] Mauri, G., Williams-Jones, G. & Saracco, G., *Mwtmat-Application of Multiscale Wavelet Tomography on Potential Fields*, Computers & Geosciences, **37**(11), pp. 1825-1835, Nov. 2011. DOI: 10.1016/j.cageo.2011.04.005.

[27] Mauri, G., Williams-Jones, G. & Saracco, G., *Depth Determinations of Shallow Hydrothermal Systems By Self-potential and Multi-scale Wavelet Tomography*, Journal of Volcanology and Geothermal Research, **191**(3-4), pp. 233-244, Apr. 2010. DOI: 10.1016/j.jvolgeores.2010.02.004.

[28] Burrus, C.S., Gopinath, R.A. & Guo, H., *Introduction to Wavelets and Wavelet Transforms: A Primer, 1st edition,* Upper Saddle River, N.J.: Pearson, 1997.

[29] Mallat, S., *A Wavelet Tour of Signal Processing*, Third Edition: The Sparse Way, Amsterdam; Boston: Academic Press, 2008.

[30] Moreau, F., Gibert, D., Holschneider, M. & Saracco, G., *Wavelet Analysis of Potential Fields*, Inverse Problems, **13**(1), p. 165, 1997. DOI: 10.1088/0266-5611/13/1/013.

[31] Saracco, G., Labazuy, P. & Moreau, F., *Localization of Self-Potential Sources in Volcano-Electric Effect with Complex Continuous Wavelet Transform and Electrical Tomography Methods for an Active Volcano*, Geophys. Res. Lett., **31**(12), p. L12610, Jun. 2004. DOI: 10.1029/2004GL019554.

[32] Mallat, S. & Hwang, W.L., *Singularity Detection and Processing with Wavelets*, IEEE Transactions on Information Theory, **38**(2), pp. 617-643, Mar. 1992. DOI: 10.1109/18.119727.

[33] Saracco, G., Arneodo, A., Beylkin, G. , Fedi, M., Cella, F., Quarta, T. & Villani, A.V., *Special Issue on Continuous Wavelet Transform in Memory of Jean Morlet, Part II2D Continuous Wavelet Transform of Potential Fields Due to Extended Source Distributions*, Applied and Computational

Harmonic Analysis, **28**(3), pp. 320-337, May 2010. DOI: 10.1016/ j.acha.2010.03.002.

[34] Loke, M.H., Acworth, I. & Dahlin, T., *A Comparison of Smooth and Blocky Inversion Methods in 2D Electrical Imaging Surveys*, Exploration Geophysics, **34**, pp. 182-187, Jan. 2003. DOI: 10.1071/EG03182.

[35] Kim, J.H., Supper, R., Tsourlos, P., & Yi, M.J., *4D Inversion of Resistivity Monitoring Data through Lp Norm Minimizations*, Geophysical Journal International, **195**(3), pp. 1640-1656, Dec. 2013. DOI: 10.1093/gji/ggt324

[36] Borsic, A. & Adler, A., *A Primal–Dual Interior-Point Framework for Using the L1 Or L2 Norm on the Data and Regularization Terms of Inverse Problems*, Inverse Problems, **28**(9), 095011, Sep. 2012. DOI: 10.1088/ 0266-5611/28/9/095011.

[37] Al-Saigh, N.H., Mohammed, Z.S. & Dahham, M.S., *Detection of Water Leakage from Dams by Self-Potential Method*, Engineering Geology, **37**(2), pp. 115-121, Jun. 1994. DOI: 10.1016/0013-7952(94)90046-9.

[38] Bolève, A., Janod, F., Revil, A., Lafon, A. & Fry, J.J., *Localization and Quantification of Leakages in Dams Using Time-Lapse Self-Potential Measurements Associated with Salt Tracer Injection*, Journal of Hydrology, **403**(3-4), pp. 242-252, Jun. 2011. DOI: 10.1016/j.jhydrol. 2011.04.008.

[39] Jardani, A., Revil, A., Bolève, A. & Dupont, J.P., *Three-Dimensional Inversion of Self-Potential Data Used to Constrain the Pattern of Groundwater Flow in Geothermal Fields*, J. Geophys. Res., **113**(B9), pp. B09204, Sep. 2008. DOI: 10.1029/2007JB005302.

[40] Saracco, G., Mathé, P.É., Moreau, F. & Hermitte, D., *Localization and Characterization of Buried Magnetic Structures Using a Multi-Scale Tomography. Application to Archaeological Structures on Fox-Amphoux Site*, ArcheoSciences. Revue d'archéométrie, **33**(suppl.), pp. 339-343, Oct. 2009. DOI: 10.4000/archeosciences.1806.

[41] Soueid Ahmed, A., Jardani, A., Revil, A. & Dupont, J.P., *SP2DINV: A 2D Forward and Inverse Code for Streaming Potential Problems*, Computers & Geosciences, **59**, pp. 9-16, Sep. 2013. DOI: 10.1016/ j.cageo.2013.05.008.

[42] Sungkono, *Robust Interpretation of Single and Multiple Self-Potential Anomalies via Flower Pollination Algorithm*, Arabian Journal of Geosciences, **13**(100), 2020. DOI: 10.1007/s12517-020-5079-4.

[43] Abdelazeem, M., Gobashy, M., Khalil, M.H. & Abdrabou, M., *A Complete Model Parameter Optimization from Self-Potential Data Using Whale Algorithm*, Journal of Applied Geophysics, **170**, 103825, Nov. 2019. DOI: 10.1016/j.jappgeo.2019.103825.

[44] Husein, A., Sungkono, Wijaya, A. & Hadi, S., *Subsurface monitoring of P.79 - P.82 LUSI Embankment using GPR Method to Locate Subsidence and Possible Failure*, in 15th International Conference on Ground

Penetrating Radar (GPR), Brussels, Belgium, pp. 268-273, Jul. 2014. DOI: 10.1109/ICGPR.2014.6970427.

[45] Husein, A., Mazzini, A., Lupi, M., Mauri, G., Kemna, A., Santosa, B.J. & Hadi, S., *Investigating the Watukosek Fault System Using Combined Geophysical Methods Around Lusi Eruption Site*, **19**, 12266, Apr. 2017.

[46] Team Work of Operational Planning, TTG and BM Monitoring Activity, *Center of Mud Volcano Control*, Year-end Report, 2018. (Text in Indonesia)